EDGE ARTICLE

Check for updates

Ion polarisation-assisted hydrogen-bonded ferroelectrics in liquid crystalline domains†

Guohao Yuan, [ab] Yuko Kimura, [a] Takayuki Kobayashi, [a] Takashi Takeda, [ID] [ab] Norihisa Hoshino [ID] [ab] and Tomoyuki Akutagawa [ID] *[abc]

An alkylamide-substituted ($-NHCOC_{10}H_{21}$) hydrogen-bonded dibenzo[18]crown-6 derivative (**1**) was prepared to stabilise the ionic channel structure in a discotic hexagonal columnar (Col_h) liquid crystal. The introduction of simple M^+X^- salts such as $Na^+PF_6^-$ and K^+I^- into the ionic channel of **1** enhanced the ionic conductivity of the Col_h phase of the $M^+ \cdot (1) \cdot X^-$ salts, with the highest ionic conductivity reaching $\sim 10^{-6}$ S cm^{-1} for $K^+ \cdot (1) \cdot I^-$ and $Na^+ \cdot (1) \cdot PF_6^-$ at 460 K, which was approximately 5 orders of magnitude higher than that of **1**. The introduction of non-ferroelectric **1** into the ferroelectric N,N',N''-tri(tetradecyl)-1,3,5-benzenetricarboxamide (**3BC**) elicited a ferroelectric response from the mixed Col_h phase of $(3BC)_x(1)_{1-x}$ with $x = 0.9$ and 0.8. The further doping of M^+X^- into the ferroelectric Col_h phase of $(3BC)_{0.9}(1)_{0.1}$ enhanced the ferroelectric polarisation assisted by ion displacement in the half-filled ionic channel for the vacant dibenzo[18]crown-6 of $(3BC)_{0.9}[(M^+)_{0.5} \cdot (1) \cdot (X^-)_{0.5}]_{0.1}$.

Introduction

Intermolecular hydrogen-bonding interactions have been used for the association and dissociation of each molecule in flexible and transformable molecular-assembly structures,[1] which are used in the formation of biological structures.[2] Among the various types of hydrogen-bonding interaction, amide-type intermolecular hydrogen-bonding interactions ($=O\cdots N-H-$) play an important role in the formation of biological molecular assembly structures such as α-helixes and β-sheets in polypeptides, collagen, and keratin.[2,3] The bonding energy of amide-type hydrogen-bonding interactions is typically in the range of 5–10 kJ mol^{-1}; therefore, the structural reconstruction of proteins in biological systems is effectively activated by both the association and dissociation processes of each molecule in flexible molecular assemblies.[1–4] Such amide-type intermolecular hydrogen-bonding interactions are also useful for the construction of functional supramolecular assemblies.[5,6] For instance, the one-dimensional (1D) $=O\cdots N-H-$ hydrogen-bonding interaction has been effectively utilised for constructing low-dimensional molecular assembly structures.[7–9] Moreover, a typical 1D molecular assembly has been reported in the discotic liquid crystal phase of a benzene derivative bearing multiple hydrophobic alkylamide ($-CONHC_nH_{2n+1}$) chains, where the effective intermolecular hydrogen-bonding interactions formed a 1D hydrogen-bonded π-stacking columnar assembly that further assembled into a discotic hexagonal columnar (Col_h) liquid crystal phase.[10] The 1D intermolecular $=O\cdots N-H-$ hydrogen-bonding interactions can also form nanofibers and organogels,[11–14] wherein the three-dimensional (3D) entanglement of each 1D fibrous molecular assembly generates micropores that capture the solvents in the organogel state. An excellent organogellation ability has been reported for cyclohexane-1,2-dialkylamide and benzene-1,3,5-trialkylamide derivatives.[14–17] Thus, hydrogen-bonded alkylamide chains are one of the interesting functional units that can form flexible 1D supramolecular assemblies such as Col_h liquid crystals, organogels, and nanofibers.

The formation of organogels in CH_2Cl_2, N,N-dimethylformamide (DMF), dimethyl sulfoxide (DMSO), nitrobenzene, and benzonitrile has been reported for N,N',N''-tri(octadecyl)-1,3,5-benzenetricarboxamide,[18,19] which forms π-stacking 1D molecular assemblies through intermolecular $=O\cdots N-H-$ hydrogen-bonding interactions.[20–25] The formation of a Col_h liquid crystal phase has been reported for a symmetrical three-chain system of N,N',N''-trialkyl-1,3,5-benzenetricarboxamide.[10] The introduction of three $-CONHC_nH_{2n+1}$ chains into the benzene core effectively generates intermolecular interactions to form the Col_h phase. The π-stacking columns, aided by the intermolecular $=O\cdots N-H-$ hydrogen-bonding interactions, have been characterized by the single-crystal X-ray diffraction analysis of N,N',N''-trimethyl-1,3,5-benzenetricarboxamide and N,N',N''-trimethoxyethyl-1,3,5-

[a]*Graduate School of Engineering, Tohoku University, Sendai 980-8579, Japan. E-mail: akutagawa@tohoku.ac.jp*

[b]*Institute of Multidisciplinary Research for Advanced Materials (IMRAM), Tohoku University, 2-1-1 Katahira, Aoba-ku, Sendai 980-8577, Japan*

[c]*National Institute for Material Science (NIMS), 1-2-1 Tsukuba, 305-0047, Japan*

† Electronic supplementary information (ESI) available: Experimental; thermal stability and TG charts; vibrational IR spectra of molecule **1** and $M^+ \cdot (1) \cdot X^-$; PXRD profiles of $M^+ \cdot (1) \cdot X^-$ salts; temperature-dependent $Z'–Z''$ plots of $M^+ \cdot (1) \cdot X^-$ salts; POM images of $(3BC)_{1-x}(1)_x$. See DOI: 10.1039/d1sc03301h

© 2021 The Author(s). Published by the Royal Society of Chemistry

benzenetricarboxamide.[26–28] For these hydrogen-bonded 1D supramolecular assemblies, the interesting physical response of ferroelectric switching has been reported in the Col_h phase of N,N',N''-trialkyl-1,3,5-benzenetricarboxamide, which generated polarisation–electric field (P–E) hysteresis curves, typical of the ferroelectric ground state.[29–32] The 1D intermolecular =O···N–H– hydrogen-bonded interactions along the π-stacking direction can be inverted by applying an external electric field, which results in dipole inversion and ferroelectricity. The two different hydrogen-bonding orientations (=O···N–H– and –N–H···O=) along the π-stacking axis can transform into each other under the application of an outer electric field.[33–37]

Another type of interesting molecular system with a selective ion recognition ability has been extensively designed with crown ether derivatives for application in phase-transfer catalysis, ion separation, ion sensing, and ion transport in the solution phase.[38] The chemical designs of the pore environment such as [12]crown-4, [15]crown-5, and [18]crown-6 are useful because of their high affinity to Li^+, Na^+, and K^+ ions.[39] In the solid state, a regular array of crown ether can form a 1D ionic channel by the regular overlapping of the central cavity. Simple ionic channel structures such as $(Li^+)_x([15]crown-5)$, $(Li^+)_x([18]crown-6)$, and $(Na^+)_x([18]crown-6)$ can coexist with an electrically conducting π-stacking column of $[Ni(dmit)_2]$ molecules in the highly electrically conducting single-crystals of $(Li^+)_x([15]crown-5)[Ni(dmit)_2]_2$, $(Li^+)_x([18]crown-6)[Ni(dmit)_2]_2$, and $(Na^+)_x([18]crown-6)[Ni(dmit)_2]_2$, where the motional freedom of Li^+ ions is coupled with the conduction electrons.[40,41] In addition, crown ether fused liquid crystalline phthalocyanine derivatives have been prepared to fabricate ionic channels, where the cation binding 1D fibrous supramolecular assembly and π-stacking column have been reported.[42–44] The molecular frameworks of crown ethers are interesting candidates for controlling the ionic motion in a molecular assembly, which has been applied to solid state ionics.[45] Among the various types of molecular assembly, the lattice periodicity of liquid crystal phases such as nematic (N) and smectic (Sm) states is much lower than that of the single crystalline state, and the flexible molecular assembly structure enables the design of the dynamic motion of ions. Many ionic liquid crystalline materials have a relatively high ionic conductivity of up to 1.5×10^{-4} S cm^{-1} in the Sm phase at around 350 K.[46–48] Interestingly, ion-conductive liquid crystalline materials based on the diaza[18]crown-6 derivative bearing decylalkoxy-p-cyanobiphenyl chains have been reported by Espinet et al.,[49] and the introduction of K^+I^- into the crown ether imparted an ionic conductivity of 3.0×10^{-7} S cm^{-1} at 530 K, which is lower than that of a K^+-free crown ether. The lower conductivity of the K^+-doped crown ether is due to the effective K^+-capturing ability of the diaza[18]crown-6 unit and the insufficient formation of a channel-type molecular assembly in the absence of a regular array of crown ethers. Therefore, the formation of a 1D regular array of crown ethers should be one of the key points to increase the ionic mobility in molecular assemblies. Another interesting liquid crystalline material with ion-transport capability has been reported with a triphenylene π-core bearing n-alkoxy-substituted crown ethers,[50] where the ionic conductivity of the K^+I^--doped

molecular assembly was 20 times larger than that of the K^+SCN^--doped assembly and 100 times larger than that of the $K^+BF_4^-$ assembly. Therefore, the counter-anion plays an important role in controlling the K^+ conductivity in the 1D channel.[51] The liquid crystalline ion-captured M^+(crown ether) usually modifies the thermal phase transition behaviour significantly. The addition of an alkali metal salt into a mesogenic state changes it into a non-mesogenic state due to an increase in intermolecular interactions.[52–55] Among the variety of inorganic anions, the soft I^- ion can significantly stabilise the thermal liquid crystal phases.[56,57]

A combination of specific chemical structures between the hydrogen-bonded alkylamide chains and crown ether can realize an interesting 1D molecular assembly with an ionic channel, which enables the design of multi-functional molecular assemblies such as ion-conductive ferroelectrics. For instance, the ionic conductivity of organic materials is related to their mechanical, electrical, and optical properties.[58] Although the presence of ionic conductivity usually disturbs the ferroelectric polarisation due to leakage current,[59] ion-conductive ferroelectrics based on typical inorganic perovskites such as $Bi_4Ti_3O_{12}$ have been reported,[60–62] which showed a relatively high ionic conductivity of $\sim 10^{-2}$ S cm^{-1} at 923 K and a high remanent polarisation of ~ 50 μC cm^{-2} along the a–c plane at 298 K. These ion-conductive ferroelectrics with a non-linear electric response have attracted much attention for potential application in transducers, actuators, sensors, etc.[63] Although ion-conductive inorganic ferroelectrics have been developed, there is no report on organic molecular materials.

In this paper, we report the molecular design, synthesis, and physical characterization of a dibenzo[18]crown-6 derivative bearing four $-NHCOC_{10}H_{21}$ chains (1 in Scheme 1). The cavity size of 1 fits a K^+ ion well, and the four $-NHCOC_{10}H_{21}$ chains formed intermolecular =O···N–H– hydrogen-bonding interactions to generate a 1D columnar molecular assembly exhibiting both ferroelectricity and ionic conductivity. Although the
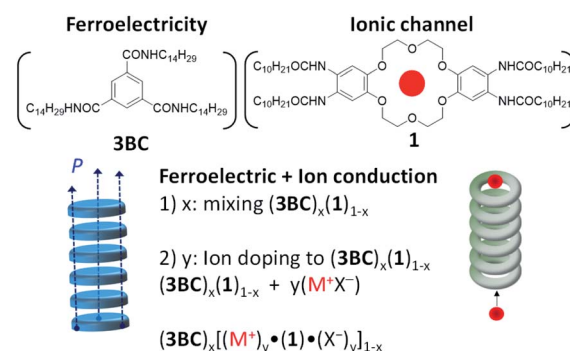
Scheme 1 Molecular structures of the alkylamide ($-NHCOC_{10}H_{21}$)-fused dibenzo[18]crown-6 derivative (1) and ferroelectric N,N',N''-tris(tetradecyl)-1,3,5-benzenetricarboxamide (3BC). 3BC and 1 formed the ferroelectric and ionic channel type Col_h phase. (1) Formation of the mixed Col_h phase of $(3BC)_x(1)_{1-x}$, where x is the mixing ratio of 3BC. (2) Formation of the M^+ doping mixed Col_h phase of $(3BC)_x[M^+_y \cdot (1) \cdot X^-_y]_{1-x}$, where y is the mixing ratio of M^+X^- per dibenzo[18]crown-6 unit in molecule 1.

formation of a 1D hydrogen-bonded columnar structure of **1** has been observed in the Col_h liquid crystal phase, no ferroelectric response was observed in the $P–E$ hysteresis curve in the Col_h phase. It has been reported that the introduction of the nearest-neighbouring $-CONHC_nH_{2n+1}$ chains on the benzene π-core suppresses the ferroelectricity due to steric hindrance to the rotation of the hydrogen-bonded alkylamide chains. In addition, the mode of substitution of $-NHCOC_nH_{2n+1}$ chains on benzene, *i.e.*, the direct bonding of the nitrogen atom with the benzene π-core, suppresses the ferroelectric response due to the steric hindrance to rotation. The ferroelectric response was unfortunately suppressed in the Col_h phase of **1**. Therefore, we first evaluated the ion-doping effect for **1** to control the ionic conduction behaviour of the $M^+ \cdot (1) \cdot X^-$ system, where $M^+ = Na^+$, K^+, and Cs^+ and $X^- = Br^-$, I^-, PF_6^-, SCN^-, and CH_3COO^-. To induce ferroelectricity, we fabricated mixed liquid crystals of **1** and N,N',N''-tris(tetradecyl)-1,3,5-benzenetricarboxamide (**3BC** in Scheme 1) wherein the 1D ionic channel of **1** and the 1D ferroelectric hydrogen-bonded chains of **3BC** coexist as $(3BC)_x(1)_{1-x}$ (x is the mixing ratio of **3BC**). The molecular assembly structures and the dielectric and ferroelectric responses of $(3BC)_x(1)_{1-x}$ were evaluated for the mixing ratios of $x = 0.9$, 0.8, and 0.7, and the ferroelectric properties of the ion-doped mixed systems, $(3BC)_{0.9}[(Na^+)_{0.5} \cdot (1) \cdot (PF_6^-)_{0.5}]_{0.1}$, $(3BC)_{0.9}[(K^+)_{0.5} \cdot (1) \cdot (PF_6^-)_{0.5}]_{0.1}$, and $(3BC)_{0.9}[(Cs^+)_{0.5} \cdot (1) \cdot (CO_3^{2-})_{0.25}]_{0.1}$, were examined to clarify the size effect of the alkali metal ion (M^+) in the ionic channels. In the M^+ doped mixed Col_h phase of $(3BC)_x[M^+_y \cdot (1) \cdot X^-_y]_{1-x}$, y is the mixing ratio of M^+X^- per dibenzo[18]crown-6 unit in molecule **1**. Therefore, the condition of $y = 0.5$ corresponds to a half site occupation inside the ionic channel of molecule **1**, *i.e.* $M^+_{50} \cdot (1)_{100}$ for 100 dibenzo[18]crown-6 columns.

Results & discussion

Molecular assemblies and phase transition behaviour of 1 and $M^+ \cdot (1) \cdot X^-$ salts

The Col_h liquid crystal phase of **3BC** was observed in the temperature range of 320–470 K (Fig. S1a†). The intermolecular amide-type $=O \cdots N-H-$ hydrogen-bonding interaction formed a π-stacking column of $(3BC)_\infty$ with a hexagonal columnar arrangement. In contrast, four hydrogen-bonded $-NHCOC_{10}H_{21}$ chains of molecule **1** formed the same Col_h phase above 475 K, whose phase transition temperature to the Col_h phase was 155 K higher than that of **3BC** due to the high thermal stability of **1**. Before phase transition into the Col_h phase, two kinds of phase transition, S1–S2 and S2–Col_h, were observed at 380 and 475 K with transition enthalpy changes (ΔH) of 10.1 and 14.1 kJ mol^{-1}, respectively (Fig. S1a†). The Col_h phase of **1** was significantly stable compared with that of **3BC** due to the effective intermolecular hydrogen-bonding interaction between the four $-NHCOC_{10}H_{21}$ chains. The polarized optical microscope (POM) images under the cross-Nicole optical arrangement showed fluidic and birefringence behaviours for the Col_h phases of both **1** and **3BC**. A focal conic texture was observed in the POM image of **1** at 500 K (Fig. S1b†). The TG analysis of **1** revealed a high thermal stability up to 510 K (Fig. S2†), which corresponded to

a relatively narrow thermal stability of the Col_h phase of **1** from 475 to 510 K.

The formation of the hydrogen-bonded 1D molecular assembly structure was also confirmed by the formation of transparent organogels of **1** in $CHCl_3$ or toluene with a concentration of ~ 1 mM (Fig. S1c†). Molecule **1** was insoluble in CH_3OH, C_2H_5OH, THF, CH_3CN, hexane, *etc.*, and the white powder precipitated from DMF and DMSO in the absence of an organogellation behaviour. The 1D hydrogen-bonded stack of dibenzo[18]crown-6 moieties formed an ionic channel through the $=O \cdots N-H-$ hydrogen-bonding interaction (Fig. S3 and S4†), which further assembled into a 3D entangled structure with the solvent remaining in the micropores to form the organogel. The formation of the Col_h phase of **1** was confirmed from the temperature-dependent PXRD profile (Fig. S5†). One sharp diffraction peak was observed at $2\theta = 2.48°$ for the Col_h phase at 493 K, which was assigned to $d_{100} = 3.56$ nm of the hexagonal columnar lattice (Fig. S5†). The d_{100} spacing is shorter than the maximum length of molecule **1** (~ 4 nm), which is consistent with the inter-digitated molecular assembly structure of the lateral alkyl chains. The broad diffraction peak at $2\theta = 20.3°$ could be assigned to the periodicity of $d_{001} = 0.438$ nm, corresponding to the melting state of the four alkyl chains and the average stacking distance of [18]crown-6 in the Col_h phase.

The cavity size of [18]crown-6 in **1** fitted the K^+ cation well, forming a stable K^+-inclusion complex, $K^+ \cdot (1)$, which requires a counter-anion (X^-) to compensate for the total charge of the $K^+ \cdot (1) \cdot X^-$ salt (Table S1†). The molecular structure of X^- also affected the thermal phase transition behaviour of the Col_h and isotropic liquid (I.L.) phases; therefore, we first evaluated the TG and DSC profiles of the five kinds of $K^+ \cdot (1) \cdot X^-$ salt with $X^- = Br^-$, I^-, PF_6^-, SCN^-, and CH_3COO^-. The structural modification of X^- from symmetrical (Br^-, I^-, and PF_6^-) to linear (SCN^- and CH_3COO^-) anions affects the formation of the Col_h phase. Furthermore, the cation size affects the ion-inclusion ability of [18]crown-6 although the size-fitted $K^+ \cdot (1) \cdot X^-$ is the most tightly bound supramolecular assembly structure. From these points of view, we fabricated two different salts, $Na^+ \cdot (1) \cdot PF_6^-$ and $Cs^+ \cdot (1) \cdot (CO_3^{2-})_{0.5}$, where the Na^+ and Cs^+ cations of $Na^+ \cdot (1) \cdot X^-$ and $Cs^+ \cdot (1) \cdot (X^{2-})_{0.5}$ salts were weakly bound in the cavity of [18]crown-6 in contrast to $K^+ \cdot (1) \cdot X^-$. Here, a half amount of $Cs^+_2CO_3^{2-}$ was utilised to compensate for the occupation state in the ionic channel and total charge. Another important point is the mixing ratio of M^+X^- into the Col_h phase of **1**; different mixing ratios of $(K^+)_y \cdot (1) \cdot (SCN^-)_y$ with $y = 0.3$ to 1.0 were used to evaluate the vacant ionic sites in the channel. The presence of vacant [18]crown-6 sites will enhance the ionic conductivity (σ_{ion}) compared with that of a fully K^+-occupied ionic channel.

Fig. 1a shows the DSC profiles of $K^+ \cdot (1) \cdot SCN^-$ (red) and $K^+ \cdot (1) \cdot I^-$ (blue). The phase transition from the solid to the Col_h phase was observed from the DSC profiles and POM images (Fig. 1c and d), with both fluidic and birefringence behaviours confirmed in the Col_h phase. Typical focal conic and/or spherulitic textures were observed in the Col_h mesophase of the $M^+ \cdot (1) \cdot X^-$ salts. Although the S2–Col_h phase transition
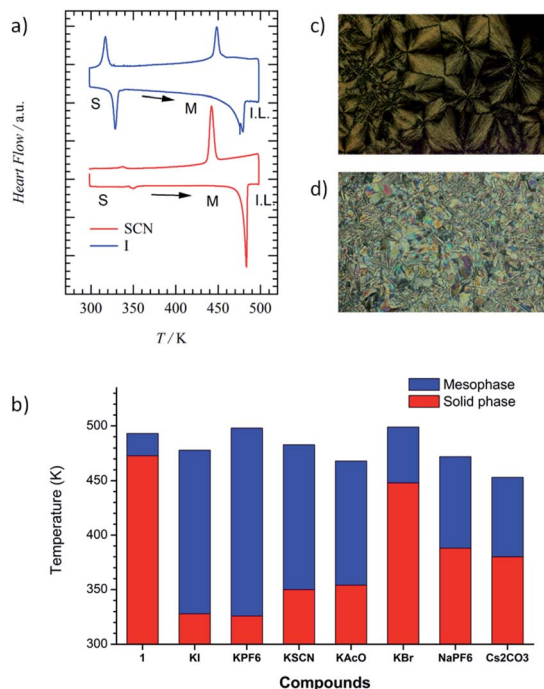
Fig. 1 Phase transition behaviour of $M^+ \cdot (1) \cdot X^-$ salts and the formation of the Col_h phase. (a) DSC profiles of $K^+ \cdot (1) \cdot SCN^-$ (red) and $K^+ \cdot (1) \cdot I^-$ (blue). (b) Temperature ranges of the solid phase (red) and Col_h phase (blue). POM images of the Col_h phase of (c) $K^+ \cdot (1) \cdot I^-$ at 483 K and (d) $K^+ \cdot (1) \cdot SCN^-$ at 473 K.

temperature of **1** was relatively high at 473 K, an equimolar addition of the M^+X^- salt into the liquid crystalline **1** decreased the phase transition temperature from the solid to the Col_h phase by approximately 50–100 K depending on the X^- anions (Table S1†). It should be noted that the introduction of the M^+X^- salt into the Col_h liquid crystalline **1** destabilised the solid phase and formed the Col_h phase over a relatively wide temperature range.

The S–Col_h phase transition temperatures of the $K^+ \cdot (1) \cdot X^-$ salts depended on the counter-anion X^-. For instance, the phase transition temperatures to the Col_h phase decreased in the order of Br^- ($T = 448$ K), AcO^- ($T = 437$ K), PF_6^- ($T = 354$ K), SCN^- ($T = 350$ K), and I^- ($T = 328$ K). In addition, the Col_h–I.L. phase transitions were clearly observed at 478 K for $K^+ \cdot (1) \cdot I^-$ and at 483 K for $K^+ \cdot (1) \cdot SCN^-$ salts (Fig. 1a). The phase transition behaviours of S–Col_h and Col_h–I.L. were not affected by the addition of a hard anion such as Br^-, but were effectively modulated by soft anions such as I^-, PF_6^-, SCN^-, and AcO^-. The phase transition behaviours of the four anions were similar to each other and showed the lowering of the S–Col_h phase transition temperature, which suggests the complete inclusion of K^+ into the [18]crown-6 cavity and a mixed state of **1** and K^+X^- forming the $K^+ \cdot (1) \cdot X^-$ salt. When the K^+ cation was replaced with a Na^+ and/or Cs^+ cation, the S–Col_h phase transition temperatures of $Na^+ \cdot (1) \cdot PF_6^-$ and $Cs^+ \cdot (1) \cdot (CO_3^{2-})_{0.5}$ were 388 and 380 K, respectively, while their Col_h–I.L. phase transitions occurred at 472 and 453 K. Therefore, almost uniform and complete Na^+ and Cs^+ capturing states in the absence of domain

separation were confirmed in the Col_h phases of both $Na^+ \cdot (1) \cdot PF_6^-$ and $Cs^+ \cdot (1) \cdot (CO_3^{2-})_{0.5}$.

The temperature-dependent PXRD profiles of the $M^+ \cdot (1) \cdot X^-$ salts were consistent with the formation of the Col_h phase. The d-spacing of the hexagonal lattice with $d_{100} = 3.9$ nm for the $M^+ \cdot (1) \cdot X^-$ salts was consistent with that of **1** with $d_{100} = 3.4$–3.9 nm at 443 K (Fig. S3†). However, the crystalline domains of inorganic M^+X^- coexisted in the $K^+ \cdot (1) \cdot Br^-$, $K^+ \cdot (1) \cdot PF_6^-$, and $K^+ \cdot (1) \cdot I^-$ salts due to the appearance of subtle sharp diffraction peaks at around $2\theta = 20°$, which indicates the domain separation of the liquid crystalline $(M^+)_y \cdot (1) \cdot (X^-)_y$ and inorganic M^+X^- salts. In contrast, the uniform mixing of M^+X^- into the ionic channel of **1** was confirmed for the $K^+ \cdot (1) \cdot SCN^-$, $K^+ \cdot (1) \cdot AcO^-$, $Na^+ \cdot (1) \cdot PF_6^-$, and $Cs^+ \cdot (1) \cdot (CO_3^{2-})_{0.5}$ salts (Fig. S6 and S7†) owing to the absence of sharp Bragg diffraction peaks for the crystalline domain of the inorganic dopant, M^+X^-.

Ionic conductivity of ion-capturing $M^+ \cdot (1) \cdot X^-$ salts

Fig. 2a and b show the anion (X^-) and cation (M^+)-dependent σ_{ion}–T plots of the $M^+ \cdot (1) \cdot X^-$ salts, respectively. Table 1 summarizes σ_{ion} at 460 K and activation energy (E_a). The temperature-dependent Cole–Cole (Z'–Z'') plots of **1** and $M^+ \cdot (1) \cdot X^-$ salts showed ideal semicircle traces corresponding to the ionic conduction behaviours (Fig. S8†). The highest σ_{ion} of $\sim 10^{-5}$ S cm^{-1} was observed for $K^+ \cdot (1) \cdot I^-$ and $Na^+ \cdot (1) \cdot PF_6^-$ before phase transition in the I.L. state (Table S2†). Additionally, the σ_{ion} of the Col_h phase was $\sim 10^{-6}$ S cm^{-1} for most of the
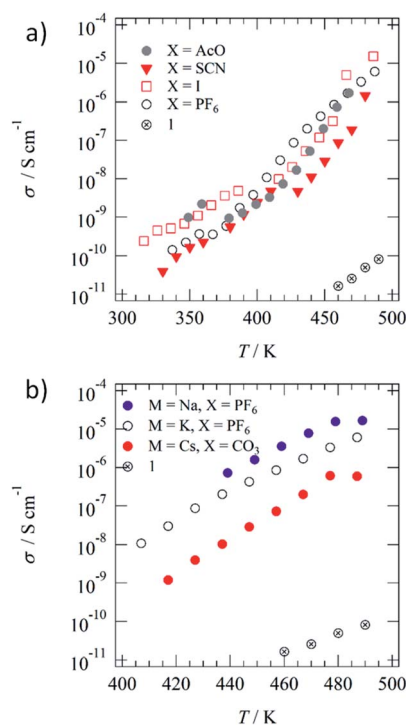

Fig. 2 Temperature-dependent ionic conductivity of $M^+ \cdot (1) \cdot X^-$. (a) Anion (X^-)-dependent σ_{K^+}–T plots of $K^+ \cdot (1) \cdot X^-$ ($X^- = AcO^-$, SCN^-, I^-, and PF_6^-) and K^+-free **1**. (b) Cation (X^-)-dependent σ_{ion}–T plots of $Na^+ \cdot (1) \cdot PF_6^-$, $K^+ \cdot (1) \cdot PF_6^-$, $Cs^+ \cdot (1) \cdot (CO_3^{2-})_{0.5}$, and M^+-free **1**.

Table 1 Ionic conductivities (σ_{ion}, S cm^{-1}) and activation energies (E_a, eV) of $(M^+)_y \cdot (\mathbf{1}) \cdot (X^-)_y$ salts

Compound	σ_{ion}, S cm^{-1} at 460 K	E_a, eV
1	1.6×10^{-11}	1.07
$K^+ \cdot (\mathbf{1}) \cdot Br^-$	9.7×10^{-9}	0.44–0.63
$K^+ \cdot (\mathbf{1}) \cdot AcO^-$	7.3×10^{-7}	0.13–2.15
$K^+ \cdot (\mathbf{1}) \cdot I^-$	4.6×10^{-6}	0.54–2.17
$K^+ \cdot (\mathbf{1}) \cdot PF_6^-$	9.2×10^{-6}	0.37–1.26
$Na^+ \cdot (\mathbf{1}) \cdot PF_6^-$	3.6×10^{-6}	1.40
$Cs^+ \cdot (\mathbf{1}) \cdot (CO_3^{2-})_{0.5}$	8.2×10^{-8}	1.70
$K^+ \cdot (\mathbf{1}) \cdot SCN^-$	8.6×10^{-8}	1.64
$(K^+)_{0.8} \cdot (\mathbf{1}) \cdot (SCN^-)_{0.8}$	7.0×10^{-7}	0.82–1.90
$(K^+)_{0.5} \cdot (\mathbf{1}) \cdot (SCN^-)_{0.5}$	9.2×10^{-7}	1.60
$(K^+)_{0.3} \cdot (\mathbf{1}) \cdot (SCN^-)_{0.3}$	9.5×10^{-8}	1.59

$K^+ \cdot (\mathbf{1}) \cdot X^-$ salts, including $X^- = AcO^-$, I^-, PF_6^-, and PF_6^-, which was approximately 6 times higher than that of M^+-free **1**. The significant increase in conductivity can be explained by the ionic transport pathway in the hydrogen-bonded array of [18] crown-6 in the $M^+ \cdot (\mathbf{1}) \cdot X^-$ salts. The K^+ conductivity (σ_{K^+}) of the $K^+ \cdot (\mathbf{1}) \cdot X^-$ salts depended on the counter-anion, X^-, which decreased in the order of I^- ($\sigma_{K^+} = 1.53 \times 10^{-5}$ S cm^{-1} at 486 K), PF_6^- ($\sigma_{K^+} = 6.10 \times 10^{-6}$ S cm^{-1} at 487 K), AcO^- ($\sigma_{K^+} = 1.73 \times 10^{-6}$ S cm^{-1} at 469 K), SCN^- ($\sigma_{K^+} = 1.46 \times 10^{-6}$ S cm^{-1} at 480 K), and Br^- ($\sigma_{K^+} = 2.30 \times 10^{-8}$ S cm^{-1} at 490 K). The σ_{K^+} of the crystalline $K^+ \cdot (\mathbf{1}) \cdot Br^-$ salt with domain separation was 3 orders of magnitude lower than that of the $K^+ \cdot (\mathbf{1}) \cdot I^-$ salt, where the mixing state of the counter-anion, X^-, affected the phase transition behaviour and σ_{K^+}. The X^- anions were bound to the positively charged K^+(dibenzo[18]crown-6) unit through electrostatic interaction, where the size and affinity of X^- anions to the cationic crown ether affected the σ_{K^+}.

Both the S–Col$_h$ and Col$_h$–I.L. phase transition temperatures of the $K^+ \cdot (\mathbf{1}) \cdot X^-$ salts decreased by the K^+-inclusion array of [18]crown-6 units compared with that of M^+-free **1**, which indicates a decrease in the intermolecular interaction between the hydrogen-bonded $K^+ \cdot \mathbf{1}$ columns. The inclusion of K^+ into the ionic channel increased the σ_{K^+}, compared with that of the M^+-free ionic channel of **1**. The size-matching K^+ ion in the cavity of dibenzo[18]crown-6 effectively stabilised the supramolecular structure of K^+(dibenzo[18]crown-6), which was further connected by the four $=O \cdots H–N–$ amide-type hydrogen-bonding interactions along the 1D molecular assembly of the ionic channel. The presence of X^- anions between the thermally melting hydrogen-bonded 1D columns decreased the intermolecular van der Waals interaction between the alkyl chains in the Col$_h$ phase, which also decreased the Col$_h$–I.L. phase transition temperature. In contrast, the addition of K^+ into the ionic channel destabilised the 1D columnar assembly due to the electrostatic $K^+ \cdots K^+$ repulsive interaction, which decreased the Col$_h$–I.L. phase transition temperature. The almost complete melting and mixing state of soft X^- anions such as I^- and PF_6^- decreased the intermolecular interaction of the crystal state, which destabilised the solid phase and lowered the S–Col$_h$ phase transition temperature.

Fig. 2b summarizes the cation (Na^+, K^+, and Cs^+)-dependent σ_{ion}–T plots of $Na^+ \cdot (\mathbf{1}) \cdot PF_6^-$, $K^+ \cdot (\mathbf{1}) \cdot PF_6^-$, and $Cs^+ \cdot (\mathbf{1}) \cdot (CO_3^{2-})_{0.5}$ salts. The Na^+ conductivity (σ_{Na^+}) of the $Na^+ \cdot (\mathbf{1}) \cdot PF_6^-$ salt ($\sigma_{Na^+} = 1.7 \times 10^{-5}$ S cm^{-1} at 487 K) was approximately 3 and 30 times larger than those of $K^+ \cdot (\mathbf{1}) \cdot PF_6^-$ ($\sigma_{K^+} = 6.1 \times 10^{-6}$ S cm^{-1} at 489 K) and $Cs^+ \cdot (\mathbf{1}) \cdot (CO_3^{2-})_{0.5}$ ($\sigma_{Cs^+} = 5.9 \times 10^{-7}$ S cm^{-1} at 487 K), respectively. A much smaller cation effectively increases the σ_{ion} due to the high carrier mobility. The size-matching K^+ ion in the ionic channel was tightly bound in the cavity of [18] crown-6, while the slightly smaller Na^+ in the Na^+([18]crown-6) ionic channel had a much higher motional freedom than that of the K^+([18]crown-6) array. Therefore, σ_{Na^+} was 3 times higher than σ_{K^+}. In contrast, the ionic radius of the Cs^+ cation is much larger than the pore size of [18]crown-6, which disturbed the Cs^+ transport along the ionic channel and drastically lowered the σ_{Cs^+}. The occupancy state of the M^+ cation in the ionic channel affected the σ_{ion} values. For instance, the σ_{ion} value of the fully M^+-occupied ionic channel of an M^+([18]crown-6) array should be lower than that of a partially occupied M^+ vacant $(M^+)_x$([18] crown-6) array due to a decrease in the electrostatic $M^+ \cdots M^+$ repulsive interaction.

Herein, we evaluated the K^+ occupation (y) effect on σ_{K^+} in the ionic channel of the $(K^+)_y \cdot (\mathbf{1}) \cdot (SCN^-)_y$ salts with different amounts of K^+ cation ($y = 0.0$, 0.3, 0.5, 0.8, and 1.0). The σ_{K^+} values of $(K^+)_y \cdot (\mathbf{1}) \cdot (SCN^-)_y$ with $y = 0.0$, 0.3, 0.5, 0.8, and 1.0 at 470 K were 2.54×10^{-11}, 2.24×10^{-7}, 5.01×10^{-6}, 9.21×10^{-7}, and 1.88×10^{-7} S cm^{-1}, respectively (Fig. S9 and Table S2†). The maximum σ_{K^+} of the $(K^+)_y \cdot (\mathbf{1}) \cdot (SCN^-)_y$ salts was obtained at $y = 0.5$ with a half-filled K^+ ion in the ionic channel of $(K^+)_{0.5} \cdot (\mathbf{1}) \cdot (SCN^-)_{0.5}$, which effectively reduced the Coulomb repulsive interaction between the nearest-neighbouring K^+ ions. The σ_{K^+} value of $(K^+)_{0.5} \cdot (\mathbf{1}) \cdot (SCN^-)_{0.5}$ at 470 K was approximately 25 and 100 000 times higher than those of the fully K^+-occupied $(K^+) \cdot (\mathbf{1}) \cdot (SCN^-)$ and M^+-free **1**, respectively. The presence of a carrier and vacant M^+ ionic sites is essential for increasing the σ_{ion} along the 1D ionic channel structure.

All the $M^+ \cdot (\mathbf{1}) \cdot X^-$ salts showed similar σ_{ion} values at temperatures before the phase transition to the I.L. state, where the σ_{ion} values were dominated by the mass of the transport carrier. The σ_{Cs^+} of the $Cs^+ \cdot (\mathbf{1}) \cdot (CO_3^{2-})_{0.5}$ salt at 447 K (2.9×10^{-8} S cm^{-1}) was lower than the σ_{Na^+} of the $Na^+ \cdot (\mathbf{1}) \cdot PF_6^-$ salt at 449 K (1.6×10^{-6} S cm^{-1}) and the σ_{K^+} of the $K^+ \cdot (\mathbf{1}) \cdot AcO^-$ salt at 449 K (2.0×10^{-7} S cm^{-1}) due to the complete dissociation of the $M^+ \cdots X^-$ pair in the Col$_h$ phase. The σ_{ion} in the Col$_h$ phase is usually dominated by the thermally activated carrier hopping process between the mobile M^+ sites in the 1D ionic channel of the M^+([18]crown-6) array, where semiconducting temperature dependence is observed for all the $M^+ \cdot (\mathbf{1}) \cdot X^-$ salts. The σ_{K^+} of the $K^+ \cdot (\mathbf{1}) \cdot SCN^-$ salt at 480 K (1.46×10^{-6} S cm^{-1}) is similar to the σ_{Li^+} of a zwitterionic liquid crystal derivative of Li^+-doped bis(trifluoromethylsulfonyl)imide and propylene carbonate in the SmA phase (10^{-4} to 10^{-5} S cm^{-1})[64] and is larger than the σ_{Li^+} of a propylene carbonate-based columnar liquid crystalline material (10^{-6} to 10^{-8} S cm^{-1}).[65] The dielectric properties of ionic liquid have been theoretically discussed to predict the association–dissociation state,[66,67] which can also apply to the ionic liquid crystalline phase. The M^+ binding ability in the

ionic liquid crystal of $M^+ \cdot (1) \cdot X^-$ salts influenced the magnitude of σ_{ion}, where the diffusion of M^+ was directly associated with the σ_{ion} value.

Phase-separated Col$_h$ phase between ionic channel 1 and ferroelectric 3BC

Although molecule **1** formed the hydrogen-bonded Col$_h$ phase, ferroelectric P–E hysteresis was not observed over the measured temperature range. The rotation of the hydrogen-bonded $-NHCOC_{10}H_{21}$ chains was suppressed in the 1D array of $(1)_\infty$ due to a large steric hindrance compared with that of the $-CONHC_nH_{2n+1}$ chains. Therefore, we focused on the thermally stable Col$_h$ phase of ferroelectric **3BC** (Scheme 1) to mix with the Col$_h$ phase of ionic channel $(1)_\infty$. Although the same kinds of Col$_h$ phase can be mixed together, the question whether the hydrogen-bonded columnar **1** and **3BC** can be mixed together remains. The hydrogen-bonded infinite columns of $(1)_\infty$ and $(3BC)_\infty$ are thermally stable and form a homogeneous single column without the mixed state of $[(3BC)_x(1)_{1-x}]_\infty$, where the same molecules tend to stack together in the same 1D column. In contrast, there are two kinds of mixing state for each 1D column of $(1)_\infty$ and $(3BC)_\infty$. The first is a homogeneous random mixing state without domain separation, and the second is an inhomogeneous domain-separated mixing state.[68,69] The mixing with and without domain separation can be distinguished by the DSC and PXRD profiles of the Col$_h$ phase. When the two different hydrogen-bonded columns of $(1)_\infty$ and $(3BC)_\infty$ can coexist in the same Col$_h$ phase, interestingly, both the ionic channel and ferroelectric chain coexist.

The S–Col$_h$ and Col$_h$–I.L. phase transition temperatures were 340 and 485 K, respectively, during the heating process, while the mixed liquid crystal of $(3BC)_{0.9}(1)_{0.1}$ ($x = 0.9$) exhibited double Col$_h$–I.L. phase transition behaviours at around 474 and 480 K due to the phase-separated domains (Fig. 3a). Similarly, two S–Col$_h$ and Col$_h$–I.L. phase transition temperatures of $(3BC)_{0.8}(1)_{0.2}$ ($x = 0.8$) were observed at 333 and 341 K and 478 and 483 K, respectively, during the heating process corresponding to the phase-separated states of the two kinds of domain. The POM image of the Col$_h$ phase of $(3BC)_{0.9}(1)_{0.1}$ at 450 K exhibited a focal conic texture similar to that of **3BC** (Fig. S10†). When **1** was mixed into the Col$_h$ phase of **3BC** above $x > 0.3$, the phase-separated state between the focal conic domain of **3BC** and the homeotropic dark domain of **1** was observed in the POM images (Fig. S10†).

The PXRD profile of the Col$_h$ phase of $(3BC)_{0.9}(1)_{0.1}$ at 380 K clearly indicates the domain-separated state of ferroelectric **3BC** and ionic channel **1** due to the appearance of two low-angle diffraction peaks with d_{100} spacings of 2.7 and 3.6 nm, respectively, which were relatively consistent with the d_{100} spacing of **3BC** and **1** (Fig. 3c). The hydrogen-bonded columns of $(3BC)_\infty$ and $(1)_\infty$ were stabilised by the formation of a segregated stacking structure of the same molecules, which further assembled to form a single domain of each Col$_h$ phase. Therefore, the hydrogen-bonded columns of $(3BC)_\infty$ and $(1)_\infty$ coexisted in the domain-separated state (Fig. 3d), which was consistent with the two d_{100} spacings observed in the PXRD
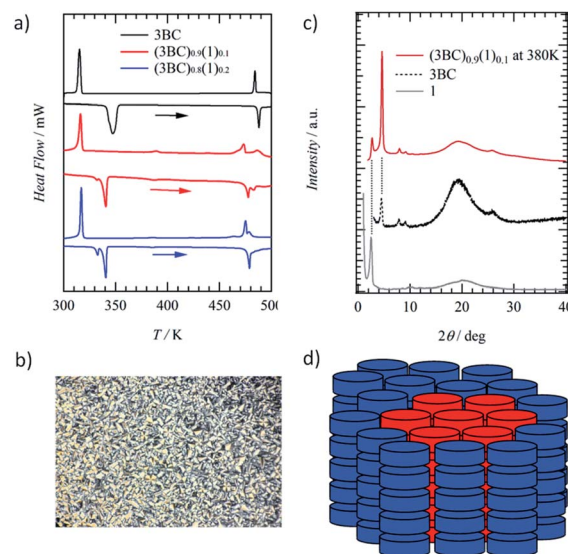

Fig. 3 Phase transition and mixed state of ionic channel $(1)_\infty$ and ferroelectric $(3BC)_\infty$ in the Col$_h$ phase. (a) DSC profiles of the mixed Col$_h$ liquid crystal of $(3BC)_x(1)_{1-x}$ with $x = 1$, 0.9, and 0.8. (b) POM image of $(3BC)_{0.9}(1)_{0.1}$ at 450 K. (c) PXRD profiles of the Col$_h$ phases of $(3BC)_{0.9}(1)_{0.1}$ at 380 K, **3BC** at 380 K, and **1** at 380 K. (d) Schematic of the phase separation state of the ferroelectric **3BC** domain (blue columns) and ionic channel **1** domain (red columns).

profile. The maximum molecular lengths of **1** and **3BC** were approximately 4.0 and 4.5 nm, respectively, assuming the all-*trans* conformations of $-NHCOC_{10}H_{21}$ and $-CONHC_{14}H_{29}$ chains. The average inter-column distances (d_{100}) of $(1)_\infty$ and $(3BC)_\infty$ in the Col$_h$ phases were shorter than those of the ideal molecular lengths, which suggests the presence of inter-digitated molecular assembly structures of alkylamide chains in the Col$_h$ phases.

Ferroelectricity of $(3BC)_x(1)_{1-x}$

Fig. 4a shows the temperature-dependent ferroelectric P–E hysteresis curves of the phase-separated Col$_h$ phases of mixed $(3BC)_{0.9}(1)_{0.1}$ together with that of **3BC**. The addition of a small amount of a similar hydrogen-bonding Col$_h$ liquid crystal usually supressed the ferroelectric response.[68,69] There was no ferroelectric response from the Col$_h$ phase of **1**, while the introduction of **1** into the ferroelectric **3BC** domain gave rise to P–E hysteresis curves. The remanent polarisation (P_r) of **3BC** at 353 K ($f = 1$ Hz) was $P_r = 1.1$ μC cm^{-2} (Fig. S11†), while the P_r of mixed $(3BC)_{0.9}(1)_{0.1}$ at 353 K was approximately 56% lower (0.48 μC cm^{-2}) than that of pure **3BC**.

The further introduction of **1** into **3BC** in mixed $(3BC)_{0.8}(1)_{0.2}$ effectively lowered the P_r to 0.26 μC cm^{-2} at 373 K (Fig. S12†), which is 24% of the initial P_r of **3BC**. The introduction of non-ferroelectric **1** into ferroelectric **3BC** drastically suppressed the ferroelectric P–E responses due to the phase-separated domains and the reduction of inter-columnar ferroelectric interaction. Although the P_r was suppressed by the introduction of **1** into **3BC**, the coercive electric field (E_{th}) of $(3BC)_x(1)_{1-x}$ was the same as that of **3BC**. Fig. 4b shows the mixing ratio (x) *vs.* P_r plots of
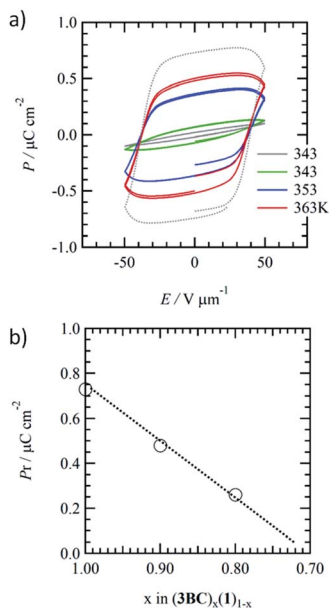
Fig. 4 Temperature-dependent $P–E$ hysteresis curves of Col_h phases for mixed crystals of (a) $(3BC)_{0.9}(1)_{0.1}$ and (b) plot of mixing ratio (x) vs. P_r of $(1)_x(3BC)_{1-x}$.

Fig. 5 Temperature-dependent $P–E$ hysteresis curves of ion-doped mixed crystals of (a) $(3BC)_{0.9}[(Na^+)_{0.5}\cdot(1)\cdot(PF_6^-)_{0.5}]_{0.1}$, (b) $(3BC)_{0.9}[(K^+)_{0.5}\cdot(1)\cdot(PF_6^-)_{0.5}]_{0.1}$, and (c) $(3BC)_{0.9}[(Cs^+)_{0.5}\cdot(1)\cdot(CO_3^{2-})_{0.25}]_{0.1}$. (d) Temperature-dependent P_r values of Na^+, K^+, and Cs^+-doped $(3BC)_{0.9}(1)_{0.1}$.

mixed $(3BC)_x(1)_{1-x}$. A linear correlation was observed for a mixing ratio of $x = 1$ to 0.8. With the addition of 30% **1** ($(3BC)_{0.7}(1)_{0.3}$), the ferroelectric response completely disappeared, which was consistent with the extrapolation in the linear $x–P_r$ plots.

Ferroelectricity of ion-doped $(3BC)_{0.9}[(M^+)_y\cdot(1)\cdot(X^-)_y]_{0.1}$

The doping effect of M^+X^- on the ferroelectric $P–E$ response of the mixed Col_h phase of $(3BC)_{0.9}(1)_{0.1}$ ($x = 0.9$) was evaluated to fabricate ion-conductive organic ferroelectrics. The motional freedom of the M^+ cation in the ionic channel $(1)_\infty$ coexisting with the ferroelectric domain of **3BC** affects the ferroelectric $P–E$ response of the mixed Col_h phase of $(3BC)_{0.9}(1)_{0.1}$.

We introduced three kinds of cation, Na^+, K^+, and Cs^+, into the ionic channel of $(3BC)_{0.9}(1)_{0.1}$ to form three ion-doped salts, $(3BC)_{0.9}[(Na^+)_{0.5}\cdot(1)\cdot(PF_6^-)_{0.5}]_{0.1}$, $(3BC)_{0.9}[(K^+)_{0.5}\cdot(1)\cdot(PF_6^-)_{0.5}]_{0.1}$, and $(3BC)_{0.9}[(Cs^+)_{0.5}\cdot(1)\cdot(CO_3^{2-})_{0.25}]_{0.1}$. The three kinds of cation (Na^+, K^+, and Cs^+) have different dynamic behaviours according to the cation size; the mobility of the Na^+ cation was higher than that of K^+ and the larger Cs^+ cation could not pass through the cavity of [18]crown-6. The occupancy states of Na^+, K^+, and Cs^+ cations in the ionic channel were fixed as 50% probability (a half site in the ionic channel) to maintain enough mobile environments. The difference in the dynamic behaviours of the cations was evaluated from the $P–E$ hysteresis responses of the mixed Col_h phase. Fig. 5a–c show the temperature-dependent $P–E$ hysteresis curves of the mixed Col_h phase of $(3BC)_{0.9}[(Na^+)_{0.5}\cdot(1)\cdot(PF_6^-)_{0.5}]_{0.1}$, $(3BC)_{0.9}[(K^+)_{0.5}\cdot(1)\cdot(PF_6^-)_{0.5}]_{0.1}$, and $(3BC)_{0.9}[(Cs^+)_{0.5}\cdot(1)\cdot(CO_3^{2-})_{0.25}]_{0.1}$, respectively. The P_r of all the ion-doped salts increased with increasing temperature, and the
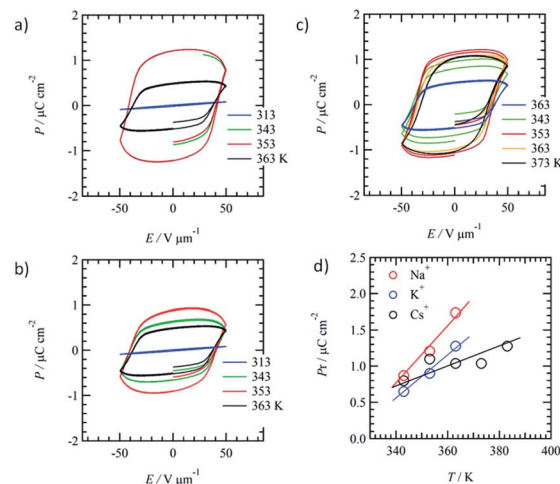
maximum P_r values of $(3BC)_{0.9}[(Na^+)_{0.5}\cdot(1)\cdot(PF_6^-)_{0.5}]_{0.1}$, $(3BC)_{0.9}[(K^+)_{0.5}\cdot(1)\cdot(PF_6^-)_{0.5}]_{0.1}$, and $(3BC)_{0.9}[(Cs^+)_{0.5}\cdot(1)\cdot(CO_3^{2-})_{0.25}]_{0.1}$ salts were 1.2 μC cm^{-2} at 353 K, 1.1 μC cm^{-2} at 363 K, and 0.9 μC cm^{-2} at 353 K, respectively.

Fig. 5d shows the temperature-dependent P_r of the Na^+, K^+, and Cs^+-doped $(3BC)_{0.9}[(Na^+)_{0.5}\cdot(1)\cdot(PF_6^-)_{0.5}]_{0.1}$, $(3BC)_{0.9}[(K^+)_{0.5}\cdot(1)\cdot(PF_6^-)_{0.5}]_{0.1}$, and $(3BC)_{0.9}[(Cs^+)_{0.5}\cdot(1)\cdot(CO_3^{2-})_{0.25}]_{0.1}$ salts. Although the P_r values of the three salts at 343 K were almost the same at ~0.7 μC cm^{-2}, the P_r values increased with increasing temperature in the order $Na^+ > K^+ > Cs^+$. At 363 K, the P_r values of $(3BC)_{0.9}[(Na^+)_{0.5}\cdot(1)\cdot(PF_6^-)_{0.5}]_{0.1}$, $(3BC)_{0.9}[(K^+)_{0.5}\cdot(1)\cdot(PF_6^-)_{0.5}]_{0.1}$, and $(3BC)_{0.9}[(Cs^+)_{0.5}\cdot(1)\cdot(CO_3^{2-})_{0.25}]_{0.1}$ were 1.74, 1.28, and 1.04 μC cm^{-2}, which indicate the different dynamic behaviours of the cations at high temperatures.

The remanent polarisation (P_r) of **3BC** at 353 K ($f = 1$ Hz) was 1.1 μC cm^{-2} (Fig. S11†), while the P_r of mixed $(3BC)_{0.9}(1)_{0.1}$ at 353 K was approximately 56% lower (0.48 μC cm^{-2}) than that of pure **3BC**. The further introduction of **1** into **3BC** in mixed $(3BC)_{0.8}(1)_{0.2}$ effectively lowered the P_r to 0.26 μC cm^{-2} at 373 K (Fig. S12†), which is 24% of the initial P_r of **3BC**. The introduction of non-ferroelectric **1** into ferroelectric **3BC** drastically suppressed the ferroelectric $P–E$ responses due to the phase-separated domains and the reduction of inter-columnar ferroelectric interaction. Although the P_r was suppressed by the introduction of **1** into **3BC**, the E_{th} of $(3BC)_{0.9}(1)_{0.1}$ was the same as that of **3BC**.

The difference in the P_r values of the three salts was discussed from the viewpoint of a possible dynamic behaviour of the 50%-occupied Na^+, K^+, and Cs^+ cations (a half occupied cation for all sites) in the ionic channel of $(M^+)_{0.5}(1)$, which affected the polarisation of the $(3BC)_{0.9}[(M^+)_{0.5}\cdot(1)\cdot(X^-)_{0.5}]_{0.1}$ salts. Scheme 2 shows the possible role of the ionic transport
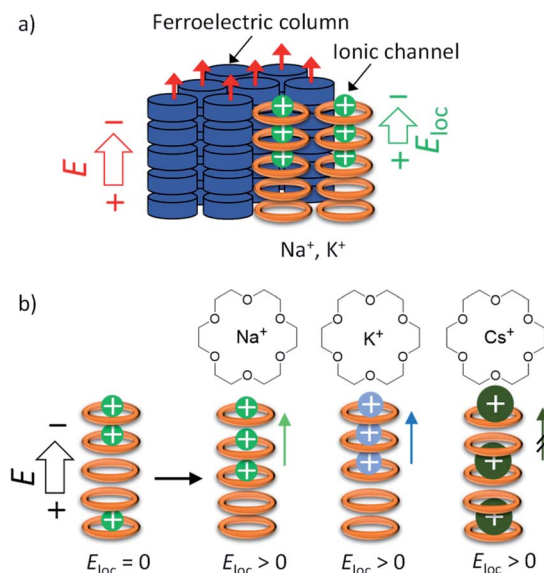
channel of **1** in the mixed Col_h phase of the $(3BC)_{0.9}[(M^+)_y \cdot (1) \cdot (X^-)_y]_{0.1}$ salts with $M^+ = Na^+$, K^+, and Cs^+. The ionic conduction along the electric field (E) can generate a local electric field (E_{loc}) along the columnar direction due to the generation of a concentration gradient of M^+ in the ionic channels, where the 50%-occupied M^+ cations in the ionic channels of $(Na^+)_{0.5}([18]crown-6)$, $(K^+)_{0.5}([18]crown-6)$, and $(Cs^+)_{0.5}([18]crown-6)$ were responsible for the electric field E. However, the dynamic behaviours of Na^+, K^+, and Cs^+ cations in the ionic channels were different. The Na^+ cation, which is smaller than the cavity of [18]crown-6, can easily modulate the Na^+ positions in the ionic channel and generate a local electric field (E_{loc}) and ionic polarisation (P_{ion}) along the applied E direction, which results in a linear paraelectric P–E correlation and contributes to the overall P_r due to the effective application of the additional E_{loc}. Although the K^+ mobility in the $(K^+)_{0.5}([18]crown-6)$ ionic channel was lower than the Na^+ mobility in the $(Na^+)_{0.5}([18]crown-6)$ channel, the application of E of a sufficient magnitude at a high-temperature region generates a concentration gradient of K^+ cations and P_{ion} along the ionic channel. Therefore, compared with the Na^+ salt, the K^+ salt exhibited a subtle weaker temperature-dependent P_r for the $(3BC)_{0.9}[(K^+)_{0.5} \cdot (1) \cdot (PF_6^-)_{0.5}]_{0.1}$ salt (Fig. 5d).

In contrast, the large Cs^+ cation could not pass through the cavity of [18]crown-6, which resulted in a small contribution to the P_{ion} term due to the subtle Cs^+ displacement along the direction of the ionic channel. Therefore, the temperature-dependent P_r enhancement for the Cs^+-doped $(3BC)_{0.9}[(Cs^+)_{0.5} \cdot (1) \cdot (CO_3^{2-})_{0.25}]_{0.1}$ salt was much smaller than those for the Na^+ and K^+-doped salts. The occupation states of Na^+ and K^+ cations under the condition of $E \neq 0$ V relaxed from the biased state to the randomly occupied M^+ state under the condition of $E = 0$ V, which also contributed to the P–E hysteresis curves with the polarisation enhancement factor of the ionic displacement effect.

Conclusions

An alkylamide-substituted ($-NHCOC_{10}H_{21}$) dibenzo[18]crown-6 derivative (**1**) was prepared to form an $=O \cdots H-N-$ amide-type hydrogen-bonding-assisted 1D ionic channel by the overlapping of the central cavity of [18]crown-6. Both the organogellation and nanofiber formation of **1** clearly supported the 1D molecular assembly structures through the $=O \cdots H-N-$ hydrogen-bonding interactions. An ionic conduction behaviour was observed for M^+X^--doped **1**, with domain-separated uniform mixing states confirmed. The highest σ_{ion} of $\sim 10^{-6}$ S cm^{-1} was obtained for the Col_h phases of $K^+ \cdot (1) \cdot I^-$ and $Na^+ \cdot (1) \cdot PF_6^-$ salts before melting into the I.L. state, whose σ_{ion} was approximately 6 orders of magnitude higher than that of M^+-free **1**. The significant σ_{ion} enhancement by the M^+X^- doping of **1** can be explained by the ionic transport along the hydrogen-bonded [18]crown-6 array. The σ_{ion} values of the $(K^+)_y \cdot (1) \cdot (SCN^-)_y$ salts were tuned to control the K^+ occupation probability, with the maximum σ_{K^+} obtained for $(K^+)_{0.5} \cdot (1) \cdot (SCN^-)_{0.5}$ wherein K^+ ions occupied 50% of the possible sites in the ionic channel, which reduced the Coulomb $K^+ \cdots K^+$ repulsive interaction. Although the phase-separated domains of non-ferroelectric **1** and ferroelectric **3BC** were observed in the mixed Col_h phase of $(3BC)_x(1)_{1-x}$, the Col_h phases at $x = 0.9$ and 0.8 showed ferroelectric P–E hysteresis responses. M^+X^- was doped into the ferroelectric Col_h phases of $(3BC)_{0.9}(1)_{0.1}$ to modulate the ferroelectric polarisation assisted by the dynamic M^+ displacements in the 50%-occupied ionic channel of $(M^+)_{0.5}(1)$. The small Na^+ cation effectively enhanced the polarisation through Na^+ transport along the ionic channel to generate a concentration gradient of Na^+ ion and ionic polarisation. A similar ionic polarisation effect was observed in the K^+-doped ionic channel of the $(3BC)_{0.9}[(K^+)_{0.5} \cdot (1) \cdot (PF_6^-)_{0.5}]_{0.1}$ salt. In contrast, the relatively low mobility of the large Cs^+ cation in the $(3BC)_{0.9}[(Cs^+)_{0.5} \cdot (1) \cdot (CO_3^{2-})_{0.25}]_{0.1}$ salt led to a subtle Cs^+ ion displacement, contributing only slightly to the overall polarisation. The ionic motion in the ionic channels can assist the ionic polarisation behaviours of the ion-conductive liquid crystalline molecular ferroelectrics. Such new kinds of multifunctional organic material have the potential to control the polarisation state in flexible memory devices.

Scheme 2 Coupling between the ferroelectricity of **3BC** and M^+-inclusion $(M^+)_{0.5}(1)$ in the mixed Col_h phase of $(3BC)_{0.9}[(M^+)_y \cdot (1) \cdot (X^-)_y]_{0.1}$ salts with $M^+ = Na^+$, K^+, and Cs^+. (a) Coexistence of the ferroelectric domain of **3BC** (blue column) and ionic channel of $(M^+)_y \cdot (1) \cdot (X^-)_y$; $M^+X^- = Na^+PF_6^-$, $K^+PF_6^-$, and $Cs^+(CO_3^{2-})_{0.5}$. The ionic conduction along the electric field (E) generates a local electric field (E_{loc}) along the columnar direction. (b) 50%-occupied $(M^+)_{0.5}([18]crown-6)$ ionic channels of $(Na^+)_{0.5}([18]crown-6)$, $(K^+)_{0.5}([18]crown-6)$, and $(Cs^+)_{0.5}([18]crown-6)$ under electric field E.

Data availability

Experimental section, TG charts, IR spectra, PXRD patterns, Z'–Z'' plots, $\log(s_{K^+})$–T^{-1} plots, POM images, and P–E hysteresis curves.

Author contributions

Y. G., Y. K., and T. K. conducted the synthetic experiments and analysed the data. T. T. performed the molecular design and preparations. N. H. carried out the dielectric measurements. T. A. prepared the manuscript and conceived the project.

Conflicts of interest

There are no conflicts to declare.

Acknowledgements

Notes and references

1 G. A. Jeffrey and W. Saenger, *Hydrogen Bonding in Biological Structures*, Springer-Verlag, Berlin, 1991.

2 *Advances in Protein Chemistry, Peptide Solvation and H−Bonds*, ed. R. L. Baldwin and D. Baker, Elsevier Academic Press, Amsterdam, *vol. 72*, 2006.

3 The Amide Linkage, A. Greenberg, C. M. Breneman and J. F. Liebman, Wiley-Interscience, New Jersey, 2003.

4 L. Stryer, *Biochemistry*, Freeman, New York, 1995.

5 G. Gilli and P. Gilli, *The Nature of the Hydrogen Bond, Outline of a Comprehensive Hydrogen bond Theory*, Oxford Univ. Press, Oxford, 2009.

6 *Supramolecular Assembly via Hydrogen Bonds I and II*, ed. D. M. P. Mingos, Springer, Berlin, 2004.

7 M. L. Bushey, T. Q. Nguyen, W. Zhang, D. Horoszewski and C. Nuckolls, *Angew. Chem., Int. Ed.*, 2004, **43**, 5446–5453.

8 T. Akutagawa, *Mater. Chem. Front.*, 2018, **2**, 1064–1073.

9 T. Akutagawa, *Bull. Chem. Soc. Jpn.*, 2021, **94**, 1400–1420.

10 Y. Matsunaga, N. Miyajima, Y. Nakayasu, S. Sakai and M. Yonenaga, *Bull. Chem. Soc. Jpn.*, 1988, **61**, 207–210.

11 R. G. Weiss and P. Terech, *Molecular Gels*, Springer, Dordrecht, 2006.

12 P. Terech and R. G. Weiss, *Chem. Rev.*, 1997, **97**, 3133–3160.

13 P. P. Bose, M. G. Drew, A. K. Das and A. Banerjee, *Chem. Commun.*, 2006, 3196–3198.

14 K. Hanabusa, M. Yamada, M. Kimura and H. Shirai, *Angew. Chem., Int. Ed.*, 1996, **35**, 1949–1951.

15 K. W. Tong, S. Dehn, J. E. Webb, K. Nakamura, F. Braet and P. Thordarson, *Langmuir*, 2009, **25**, 8586–8592.

16 Y. Shishido, H. Anetai, T. Takeda, N. Hoshino, S.-i. Noro, T. Nakamura and T. Akutagawa, *J. Phys. Chem. C*, 2014, **118**, 21204–21214.

17 B. Xing, C.-W. Yu, K.-H. Chow, P.-L. Ho, D. Fu and B. Xu, *J. Am. Chem. Soc.*, 2002, **124**, 14846–14847.

18 Y. Yasuda, E. Iishi, H. Inada and Y. Shirota, *Chem. Lett.*, 1996, **25**, 575–576.

19 K. Hanabusa, C. Koto, M. Kimura, H. Shirai and A. Kakehi, *Chem. Lett.*, 1997, **26**, 429–430.

20 A. R. Palmans, J. A. Vekemans, R. A. Hikmet, H. Fischer and E. W. Meijer, *Adv. Mater.*, 1998, **10**, 873–876.

21 L. Brunsveld, A. Schenning, M. Broeren, H. Janssen, J. Vekemans and E. W. Meijer, *Chem. Lett.*, 2000, **29**, 292–293.

22 J. Roosma, T. Mes, P. Leclère, A. R. Palmans and E. W. Meijer, *J. Am. Chem. Soc.*, 2008, **130**, 1120–1121.

23 P. J. Stals, M. M. Smulders, R. Martín-Rapún, A. R. Palmans and E. W. Meijer, *Chem.–Eur. J.*, 2009, **15**, 2071–2080.

24 S. Cantekin, D. W. Balkenende, M. M. Smulders, A. R. Palmans and E. W. Meijer, *Nat. Chem.*, 2011, **3**, 42–46.

25 C. M. Leenders, L. Albertazzi, T. Mes, M. M. Koenigs, A. R. Palmans and E. W. Meijer, *Chem. Commun.*, 2013, **49**, 1963–1965.

26 M. P. Lightfoot, F. S. Mair, R. G. Pritchard and J. E. Warren, *Chem. Commun.*, 1999, 1945–1946.

27 S. Ranganathan, K. Muraleedharan, C. C. Rao, M. Vairamani, I. L. Karle and R. D. Gilardi, *Chem. Commun.*, 2001, 2544–2545.

28 M. Kristiansen, P. Smith, H. Chanzy, C. Baerlocher, V. Gramlich, L. McCusker, T. Weber and P. Pattison, *Cryst. Growth Des.*, 2009, **9**, 2556–2558.

29 A. Sugita, K. Suzuki and S. Tasaka, *Chem. Phys. Lett.*, 2004, **396**, 131–135.

30 A. Sugita, K. Suzuki, A. Kubono and S. Tasaka, *Jpn. J. Appl. Phys.*, 2008, **47**, 1355–1358.

31 C. F. Fitié, W. C. Roelofs, M. Kemerink and R. P. Sijbesma, *J. Am. Chem. Soc.*, 2010, **132**, 6892–6893.

32 C. F. Fitié, W. C. Roelofs, P. C. Magusin, M. Wübbenhorst, M. Kemerink and R. P. Sijbesma, *J. Phys. Chem. B*, 2012, **116**, 3928–3937.

33 T. Akutagawa, T. Takeda and N. Hoshino, *Chem. Commun.*, 2021, **57**, 8378–8401.

34 H. Anetai, Y. Wada, T. Takeda, N. Hoshino, S. Yamamoto, M. Mitsuishi, T. Takenobu and T. Akutagawa, *J. Phys. Chem. Lett.*, 2015, **6**, 1813–1818.

35 H. Anetai, K. Sambe, T. Takeda, N. Hoshino and T. Akutagawa, *Chem.–Eur. J.*, 2019, **25**, 11233–11239.

36 J. Wu, T. Takeda, N. Hoshino and T. Akutagawa, *J. Phys. Chem. B*, 2020, **124**, 7067–7074.

37 H. Anetai, T. Takeda, N. Hoshino, H. Kobayashi, N. Saito, M. Shigeno, M. Yamaguchi and T. Akutagawa, *J. Am. Chem. Soc.*, 2019, **141**, 2391–2397.

38 J. Li, D. Yim, W.-D. Jang and J. Yoon, *Chem. Soc. Rev.*, 2017, **46**, 2437–2458.

39 G. W. Gokel, W. M. Lee and M. E. Weber, *Chem. Rev.*, 2004, **104**, 2723–2750.

40 T. Akutagawa, T. Hasegawa, T. Nakamura, S. Takeda, T. Inabe, K. Sugiura, Y. Sakata and A. E. Underhill, *Chem.–Eur. J.*, 2001, **7**, 4902–4912.

41 T. Nakamura, T. Akutagawa, K. Honda, A. E. Underhill, A. T. Coomber and R. H. Friend, *Nature*, 1998, **394**, 159–160.

42 C. F. van Nostrum, A. W. Bosman, G. H. Gelinck, P. G. Schouten, J. M. Warman, A. P. M. Kentgens,

M. A. C. Devillers, A. Meijerink, S. J. Picken, U. Sohling, A. –J. Schouten and R. J. M. Nolte, *Chem.–Eur. J.*, 1995, **1**, 171–182.

43 C. F. van Nostrum, S. J. Picken and R. J. M. Nolte, *Angew. Chem., Int. Ed.*, 1994, **33**, 2173–2175.

44 C. F. van Nostrum, S. J. Picken, A. –J. Schouten and R. J. M. Nolte, *J. Am. Chem. Soc.*, 1995, **117**, 9957–9965.

45 J. Sakuda, E. Hosono, M. Yoshio, T. Ichikawa, T. Matsumoto, H. Ohno, H. Zhou and T. Kato, *Adv. Funct. Mater.*, 2015, **25**, 1206–1212.

46 B. Soberats, M. Yoshio, T. Ichikawa, H. Ohno and T. Kato, *J. Mater. Chem. A*, 2015, **3**, 11232–11238.

47 T. Ohtake, Y. Takamitsu, K. Ito-Akita, K. Kanie, M. Yoshizawa, T. Mukai, H. Ohno and T. Kato, *Macromolecules*, 2000, **33**, 8109–8111.

48 V. Conejo-Rodríguez, C. Cuerva, R. Schmidt, M. Bardají and P. Espinet, *J. Mater. Chem. C*, 2019, **7**, 663–672.

49 P. Staffeld, M. Kaller, P. Ehni, M. Ebert, S. Laschat and F. Giesselmann, *Crystals*, 2019, **9**, 74–93.

50 Y. Inokuchi, O. V. Boyarkin, R. Kusaka, T. Haino, T. Ebata and T. R. Rizzo, *J. Phys. Chem. A*, 2012, **116**, 4057–4068.

51 G. X. He, F. Wada, K. Kikukawa, S. Shinkai and T. Matsuda, *J. Org. Chem.*, 1990, **55**, 541–548.

52 V. Percec, W. D. Cho, G. Ungar and D. J. Yeardley, *Chem.–Eur. J.*, 2002, **8**, 2011–2025.

53 N. Steinke, W. Frey, A. Baro, S. Laschat, C. Drees, M. Nimtz, C. Hägele and F. Giesselmann, *Chem.–Eur. J.*, 2006, **12**, 1026–1035.

54 N. Steinke, M. Jahr, M. Lehmann, A. Baro, W. Frey, S. Tussetschläger, S. Sauer and S. Laschat, *J. Mater. Chem.*, 2009, **19**, 645–654.

55 M. Kaller, S. Tussetschlager, P. Fischer, C. Deck, A. Baro, F. Giesselmann and S. Laschat, *Chem.–Eur. J.*, 2009, **15**, 9530–9542.

56 M. Kaller, C. Deck, A. Meister, G. Hause, A. Baro and S. Laschat, *Chem.–Eur. J.*, 2010, **16**, 6326–6337.

57 P. Thoniyot, M. J. Tan, A. A. Karim, D. J. Young and X. J. Loh, *Adv. Sci.*, 2015, **2**, 1400010.

58 D. M. Smyth, *Ferroelectrics*, 1994, **151**, 115–124.

59 D. V. Deyneko, D. A. Petrova, S. M. Aksenov, S. Y. Stefanovich, O. V. Baryshnikova, S. S. Fedotov, P. C. Burns, M. B. Kosmyna, A. N. Shekhovtsov and B. I. Lazoryak, *CrystEngComm*, 2019, **21**, 1309–1319.

60 H. Sun, H. J. Sohn, O. Yamamoto, Y. Takeda and N. Imanishi, *Electro. Chem. Soc.*, 1999, **146**, 1672–1676.

61 B. I. Lazoryak, O. V. Baryshnikova, S. Y. Stefanovich, A. P. Malakho, V. A. Morozov, A. A. Belik, I. A. Leonidov, O. N. Leonidova and G. V. Tendeloo, *Chem. Mater.*, 2003, **15**, 3003–3010.

62 C. Long, W. Ren, Y. Li, L. Liu, Y. Xia and H. Fan, *J. Mater. Chem. C*, 2019, **7**, 8825–8835.

63 Q. Jiang, M. N. Womersley, P. A. Thomas, J. P. Rourke, K. B. Hutton and R. C. C. Ward, *Phys. Rev. B: Condens. Matter Mater. Phys.*, 2002, **66**, 094102.

64 Y. P. Li, Y. H. R. Yang, Q. Zhao, W. C. Song, J. Han and X. H. Bu, *Inorg. Chem.*, 2012, **51**, 9642–9648.

65 H. Shimura, M. Yoshio, A. Hamasaki, T. Mukai, H. Ohno and T. Kato, *Adv. Mater.*, 2009, **21**, 1591–1594.

66 C. Held, L. F. Cameretti and G. Sadowski, *Fluid Phase Equilib.*, 2008, **270**, 87–96.

67 M. Bülow, X. Ji and C. Held, *Fluid Phase Equilib.*, 2019, **492**, 26–33.

68 H. Anetai, K. Sambe, T. Takeda, N. Hoshino and T. Akutagawa, *Chem.–Eur. J.*, 2019, **25**, 11233–11239.

69 J. Wu, T. Takeda, N. Hoshino and T. Akutagawa, *J. Phys. Chem. B*, 2020, **124**, 7067–7074.